

1 **Interface-modulated nanojunction and microfluidic platform for**
2 **photoelectrocatalytic chemicals upgrading**

3 Zhenao Gu^{a,c,1}, Xiaoqiang An^{b,1}, Ruiping Liu^b, Lunqiao Xiong^d, Junwang Tang^d,
4 Chengzhi Hu^a, Huijuan Liu^b, and Jiahui Qu^{a,c,*}

5 ^a Key Laboratory of Drinking Water Science and Technology, Research Center for Eco-
6 Environmental Sciences, Chinese Academy of Sciences, Beijing 100085, China
7 E-mail: jhqu@rcees.ac.cn

8 ^b Center for Water and Ecology, State Key Joint Laboratory of Environment Simulation
9 and Pollution Control, School of Environment, Tsinghua University, Beijing 100084,
10 China

11 ^c University of Chinese Academy of Sciences, Beijing 100049, China

12 ^d Department of Chemical Engineering, University College London, Torrington Place,
13 London, WC1E 7JE, UK.

14 ¹ These authors contributed equally to this work.

15 **Abstract:** Photoelectrocatalytic oxidation provides a technically applicable way for
16 solar-chemical synthesis, but its efficiency and selectivity are moderate. Herein, a
17 microfluidic photoelectrochemical architecture with 3-D microflow channels is
18 constructed by interfacial engineering of defective WO_3/TiO_2 heterostructures on
19 porous carbon fibers. Kelvin probe force microscopy and photoluminescence imaging
20 visually evidence the charge accumulation sites on the nanojunction. This efficient
21 charge separation contributes to 3-fold enhancement in the yield of glyceraldehyde and
22 1,3-dihydroxyacetone during glycerol upgrading, together with nearly doubled
23 production of high value-added KA oil and $\text{S}_2\text{O}_8^{2-}$ oxidant through cyclohexane and
24 HSO_4^- oxidation, respectively. More importantly, the microfluidic platform with
25 enhanced mass transfer exhibits a typical reaction selectivity of 85%, which is much
26 higher than the conventional planar protocol. Integrating this microfluidic photoanode
27 with an oxygen reduction cathode leads to a self-sustained photocatalytic fuel cell with
28 remarkably high open-circuit voltage (0.9 V) and short-circuit current (1.2 mA cm^{-2}).

29 **Keywords:** chemicals upgrading; photoelectrocatalysis; microflow channels; charge
30 separation; photocatalytic fuel cells

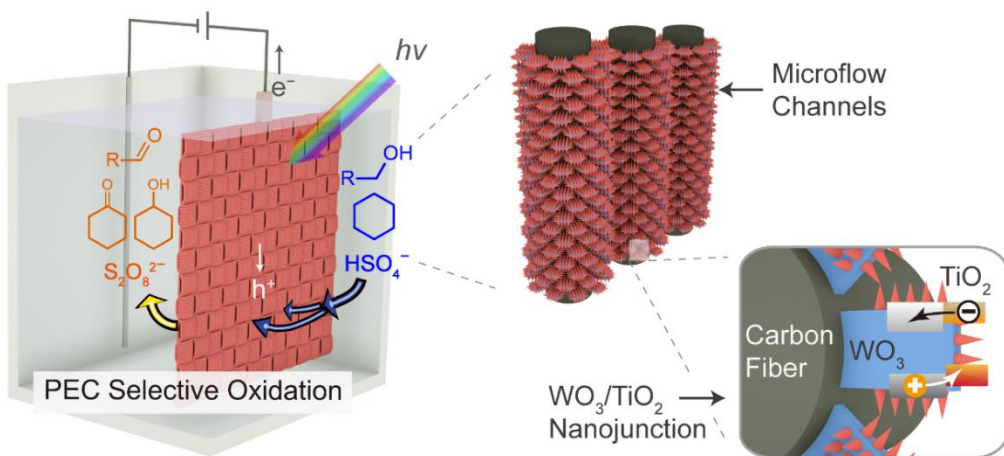
31 **1. Introduction**

Oxidative production of value-added chemicals is a fundamental transformation process in the fine chemical, pharmaceutical, biological, and agrochemical realms [1-3]. For example, the oxidation of glycerol to glyceraldehyde (GLAD) and/or 1,3-dihydroxyacetone (DHA) could essentially increase the commercial value by thousands of times [4,5]. The oxidation of other biomass-derived alcohols (benzylic alcohols and 5-hydroxymethylfurfural) [6,7], the activation of C-H bonds [8], as well as the production of various oxidizing reagents ($S_2O_8^{2-}$, ClO^- , and H_2O_2) [9] are also of significant importance for the chemical industry. However, the commonly employed thermo- and electrochemical routes not only rely greatly on adsorptive oxidants and noble metal catalysts (e.g., Pt, Pd, and Au), but also require massive energy consumption, thus seriously hindering their potential applications [3,10-12]. The alternative green oxidation process to produce valuable building-block chemicals remains one of the most important challenges of modern chemistry.

In recent years, selective organic transformation using earth-abundant semiconductors as catalysts and solar energy as the driving force has spurred tremendous research activities toward green synthesis [13-16]. Unfortunately, low quantum yields of particulate photocatalysts (<5% in most cases) and difficulties in the recovery of nanosized catalysts make the suspension systems less economically viable [17,18]. In this regard, immobilized photoelectrodes with electric-field-enhanced charge separation should be more promising for generating value-added products with low energy input. In the photoelectrochemical (PEC) processes, photon utilization and charge separation are two of the most important factors affecting the overall energy conversion efficiency. Recently, various strategies have been reported to enhance photon absorption and electron-hole separation efficiency, such as constructing multijunction structure [19-21], tuning crystal facets [22-24], as well as defect engineering [25-27]. Although promising PEC performances have been achieved, the charge transfer mechanisms remain unclear and are still under debate in many cases [28,29]. On the other hand, the mass transfer of reactants and their subsequent adsorption on the electrode surface are also essential factors determining the reaction rate and efficiency [30,31]. However, most current prevailing approaches for PEC oxidative upgrading focus on planar photoelectrodes, which suffer from low efficiency caused by limited reactants diffusion around the semiconductor-liquid interface [32-35]. Moreover, sluggish mass transfer unavoidably results in the overoxidation of valuable chemicals into undesired byproducts [36-38]. Microfluidic nanostructures can

provide new opportunities to circumvent the above drawbacks, due to the intensified mass transfer and improved reaction kinetics in the 3-D channels for precise product control [39-43]. Nevertheless, the combination of photoelectrodes with microfluidic architectures for PEC oxidative upgrading is less explored by far.

Herein, we set out to construct 3-D microfluidic PEC architecture with significantly enhanced charge and mass transfer for the oxidative upgrading of various chemicals. In such a miniaturized system, branched WO_3 nanostructures decorated by TiO_2 overlayer were used as photoactive materials, with carbon fibers as flexible, robust, and low-cost support for electron collection (Scheme 1) [44]. Kelvin probe force microscopy (KPFM) and photoluminescence imaging (PL) techniques were originally employed to visualize the spatial distribution and interfacial transfer of charge carriers in WO_3/TiO_2 heterostructures. Our results revealed that microfluidic nanojunction with oxygen vacancy defects exhibited exceptional PEC activity and selectivity for chemical upgrading reactions, such as the oxidation of glycerol and cyclohexane. We further presented the inspiring principle of self-sustainable photocatalytic fuel cell by integrating the microfluidic photoanode with an oxygen reduction cathode.



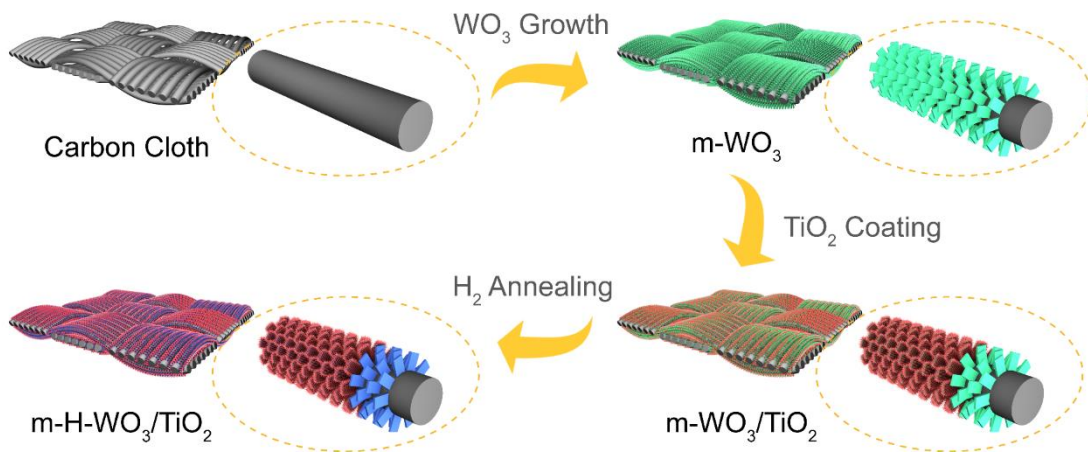
Scheme 1. Schematic diagram of the 3-D microfluidic PEC architecture with WO_3/TiO_2 nanojunction for oxidative upgrading of alcohols, hydrocarbon, and inorganic chemicals to their corresponding value-added products.

2. Experimental section

2.1 Preparation of *m-H-WO₃*

The electrode was fabricated by a seed-assisted hydrothermal method, as illustrated in Scheme 2 [45]. Briefly, a seed solution was prepared by adding 400 mg WCl_6 and 2 mL 30% H_2O_2 into 20 mL ethanol. Carbon cloth with a size of 1.5 cm × 3 cm was

dipped into the seed solution for 1 min and then dried at 40 °C for 30 min in an oven. After repeating this dip-coating process three times, the carbon cloth was annealed in air at 400 °C for 2 h. Then, 330 mg Na₂WO₄·2H₂O was dissolved in 90 mL deionized water, followed by adding 6 mL of 6 M HCl and 1.8 g oxalic acid dihydrate. After stirring for 30 min, 20 mL of the mixture was transferred into a 50 mL Teflon-lined stainless autoclave. The seeded carbon cloth was held by a self-made PTFE holder and placed vertically in the autoclave (Fig. S1). The autoclave was then sealed and heated at 180 °C for 8 h. This hydrothermal treatment was repeated one more time with a refreshed precursor solution to obtain a dense layer of WO₃. After the reaction, the carbon cloth was taken out and rinsed with deionized water. Finally, the sample was annealed in air at 500 °C for 2 h with a heating rate of 2 °C min⁻¹ and referred to as m-WO₃. To obtain defective m-WO₃ film (denoted as m-H-WO₃), the electrode was placed in a tube furnace with 50 mL min⁻¹ gas flow (10% H₂ and 90% Ar) and annealed at 350 °C for 2 h with a ramping rate of 2 °C min⁻¹. The fabrication of pl-H-WO₃ is similar to m-H-WO₃ except that the substrate is FTO conductive glass.



Scheme 2. Schematic diagram of the preparation process for m-H-WO₃/TiO₂ photoanode.

2.2 Preparation of m-H-WO₃/TiO₂

A facile wet chemical method was employed to prepare m-H-WO₃/TiO₂ [29]. In brief, m-WO₃ film was placed in an aqueous mixed solution of 30 mM ammonium hexafluorotitanate and 150 mM boric acid in a water bath at 30 °C for 24 h. Then, the film was washed with deionized water and dried at room temperature. After that, the electrode was annealed in air at 350 °C for 2 h with a ramping rate of 2 °C min⁻¹ to

1 obtain the m-WO₃/TiO₂ heterostructure. The defective m-H-WO₃/TiO₂ film was
2 obtained by replacing the air with 50 mL min⁻¹ gas flow (10% H₂ and 90% Ar).

3 *2.3 Preparation of H-WO₃/TiO₂ heterojunction for KPFM measurements*

4 Graphite was used as the conductive support for the loading of defective WO₃/TiO₂
5 heterostructure to represent the interfacial contact of WO₃ and carbon cloth. Firstly, a
6 piece of graphite plate (1 cm × 3 cm) was polished by abrasive paper and ordinary
7 printing paper to obtain a shiny surface. Then the graphite plate was placed in a Teflon-
8 lined stainless autoclave containing 2 mM Na₂WO₄·2H₂O, 70 mM HCl, and 7 mM
9 ammonium oxalate with the smooth side facing down. The autoclave was then sealed
10 and heated at 120 °C for 3 h. After the hydrothermal reaction, the sample was annealed
11 in air at 500 °C for 2 h. TiO₂ nanoplate with exposed (001) facet was prepared using a
12 well-established method [46]. In brief, 25 mL aqueous solution containing 2.67 mM
13 TiF₄ and 70 mM HF were added to a Teflon-lined autoclave, followed by heating up to
14 180 °C for 12 h. The obtained TiO₂ nanocrystals were washed several times and
15 dispersed in deionized water. Then, a certain amount of TiO₂ dispersion was drop-
16 casted onto the graphite plate with WO₃. The defective H-WO₃/TiO₂ was finally
17 obtained after annealing the sample at 350 °C for 2 h with 50 mL min⁻¹ gas flow (10%
18 H₂ and 90% Ar). For comparison, a similar WO₃/TiO₂ heterostructure without defect
19 was annealed in air to investigate the impact of oxygen vacancies on the interfacial
20 charge transfer. The similar method was used to prepare WO₃/TiO₂ samples on glass
21 for PL measurements.

22 *2.4 Characterization*

23 The morphology of samples was characterized by a scanning electron microscope
24 (SEM, JSM-7001F). Transmission electron microscopy (TEM) and the corresponding
25 energy-dispersive X-ray spectroscopy (EDS) were taken on a transmission electron
26 microscope (JEM-2100F) with an acceleration voltage of 200 kV. Electron spin
27 resonance (ESR) analysis was carried out using a Bruker E500 spectrometer. X-ray
28 diffraction (XRD) patterns were recorded on a PANalytical X-ray diffractometer with
29 Cu K α radiation. X-ray photoelectron spectroscopy (XPS) spectra were recorded on a
30 Thermo ESCALAB250Xi spectrometer with a monochromated Al-K α X-ray source.
31 The photoluminescence (PL) images of WO₃/TiO₂ heterojunction were recorded on

1 Leica TCS SP8 nanoscope with an excitation wavelength of 405 nm and emission
2 wavelengths of 450–500 nm.

3 *2.5 KPFM measurement*

4 The surface potential images were taken with a Bruker Dimension Icon system under
5 ambient atmosphere in an amplitude-modulated (AM)-KPFM mode [47]. The lift mode
6 was adopted with a lift height of 100 nm and the AC voltage was set to 0.5 V. The Pt/Ir-
7 coated Si tip (PIT-V2) was used with a spring constant of 1.5-6 N m⁻¹ and resonant
8 frequency of 50-100 kHz. The light from a 500 W Hg lamp (CEL-M500, light intensity
9 ~150 mW cm⁻²) was irradiated on the sample with a ~5° grazing angle. The surface
10 photovoltage (SPV) is the difference in the surface potential (or contact potential
11 difference, CPD) before and after illumination, defined as $SPV = CPD_{light} - CPD_{dark}$.

12 *2.6 Computational fluid dynamics (CFD) study*

13 The flow fields in the micro-channels were simulated using COMSOL Multiphysics
14 5.2. The 3-D geometry “CFD” module was used to solve the flow velocity distribution
15 in the electrodes. For the microfluidic WO₃ electrode, two parallel carbon fibers in the
16 diameter of 8 μm were separated by a distance of 4 μm. WO₃ nanoplates with the
17 dimension of 2 μm × 1 μm × 200 nm were vertically aligned on the surface of both
18 carbon fibers and FTO, with loading densities of about 1 plate per μm². The water flow
19 direction in the microfluidic system was set to be perpendicular to the plane of carbon
20 fibers, with an inlet velocity of 1 mm s⁻¹. For the planar system, water flow direction
21 was parallel to the electrode plane and the inlet velocity was also set to be 1 mm s⁻¹.

22 *2.7 Photoelectrochemical measurement*

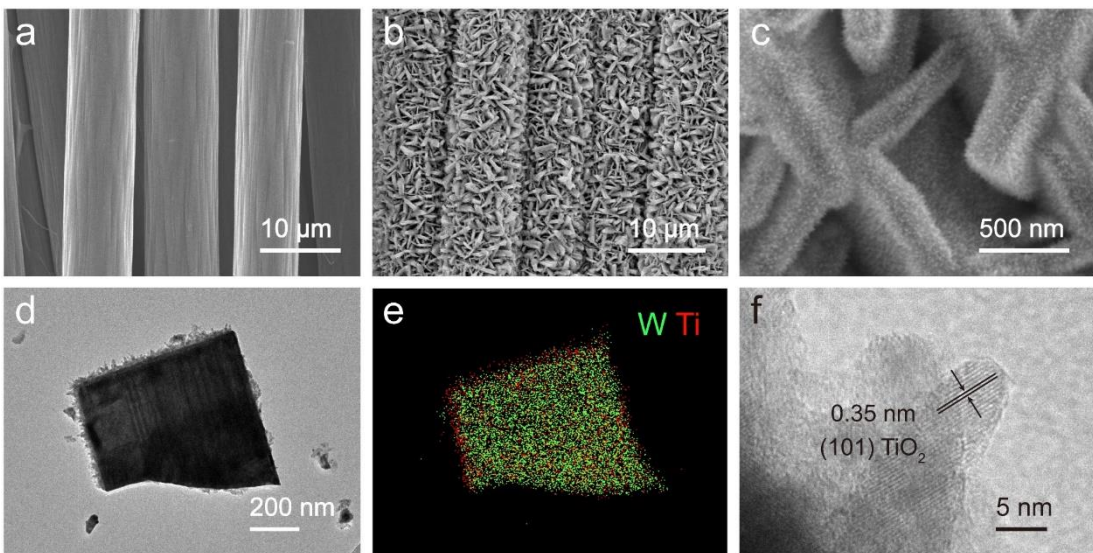
23 All the photoelectrochemical measurements were carried out on a Gamry Interface
24 1000 electrochemical workstation. For the typical three-electrode configuration, the
25 saturated Ag/AgCl electrode and Pt-wire electrode were used as the reference and
26 counter electrode, respectively. For the chemical transformation experiments, a two-
27 compartment cell was used, where the same anolyte and catholyte were separated by
28 Nafion 211 membrane. A 500 W Xe lamp (CEL-S500) coupled with an AM 1.5 G filter
29 was used to simulate solar irradiation and the light intensity was calibrated to 100 mW
30 cm⁻². Photocurrent-voltage (J–V) curves were measured at a scan rate of 5 mV s⁻¹.
31 Before data collection, the J–V scans were repeated for at least three times to reach a
32 steady state. In all the PEC experiments, oxygen was bubbled into the electrolyte with

1 a flow rate of 20 mL min⁻¹ to ensure efficient oxygen reduction reaction (ORR) and
2 mass transfer.

3 **3. Results and discussion**

4 *3.1. Structural characterization*

5 SEM image suggests that the carbon cloth substrate is comprised of an interwoven
6 network of carbon fibers (diameter \approx 8 μm) with massive microflow channels (Fig. 1a).
7 After hydrothermal growth, the staggered carbon fibers were covered with a thick layer
8 of vertically aligned WO_3 nanoplates (Fig. S2). The typical thickness and height of
9 these nanoplates are 200 nm and 2 μm , respectively. The formation of hierarchical
10 WO_3/TiO_2 nanojunctions with a high surface roughness on carbon fibers is clearly
11 revealed by Fig. 1b and 1c. According to the TEM observation, the length of TiO_2
12 nanoprickles is about 50 nm (Fig. 1d and S3). EDS elemental mapping image of m-H-
13 WO_3/TiO_2 evidences the dense and uniform wrapping of WO_3 nanoplates by TiO_2
14 branches (Fig. 1e). The uniform coverage of TiO_2 on m-H-WO₃ can be also revealed
15 by the appearance of Ti 2p peaks and substantial diminishment of W 4f signal in the
16 XPS spectra of m-H-WO₃/TiO₂ (Fig. S4). Furthermore, high-resolution TEM (HRTEM,
17 Fig. 1f) image of TiO_2 nanoparticle presents a lattice spacing of 0.35 nm, which well
18 matches up with the (101) plane of anatase TiO_2 [48]. Benefiting from the microfluidic
19 architecture and ample nanojunctions, m-H-WO₃/TiO₂ could possess higher contact
20 efficiency with the solution in comparison to its planar counterpart (Fig. S5).



21 **Fig. 1.** SEM images of (a) carbon cloth and (b,c) m-H-WO₃/TiO₂ photoanode. (d) TEM
22 image of WO_3/TiO_2 nanoplate and (e) the corresponding EDS elemental mapping
23 image. (f) HRTEM image of TiO_2 nanoparticle.
24

The crystal and electronic structure of these microfluidic electrodes were thereafter comprehensively characterized. As shown in Fig. 2a, m-H-WO₃ displays three strong XRD peaks in the range of 22°–25°, suggesting the monoclinic phase structure of WO₃ (JCPDS 89-4476). After the decoration of TiO₂, the emerging diffraction peaks at 25.3°, 37.8°, and 48.1° can be well indexed to the (101), (004), and (200) planes of anatase TiO₂ (JCPDS 21-1272). UV-visible absorption spectra of m-WO₃, m-H-WO₃, and m-H-WO₃/TiO₂ were measured and displayed in Fig. 2b. All these samples exhibit similar absorption edges of about 450 nm, corresponding to the band gap (2.7 eV) of WO₃. Compared to m-WO₃, m-H-WO₃ shows higher absorption coefficient in the visible region, which can be attributed to the formation of defect states in WO₃ [39]. For m-H-WO₃/TiO₂, there is an additional absorption edge at around 380 nm, which is in accordance with the deposition of TiO₂ (band gap of ~3.2 eV). ESR measurements were then conducted to investigate the electronic structure of m-H-WO₃/TiO₂. As displayed in Fig. 2c, both microfluidic architectures with (m-H-WO₃/TiO₂) and without TiO₂ (m-H-WO₃) exhibit strong signals at $g = 2.003$, which is a typical sign of oxygen vacancies (Fig. 2c) [25]. As this peak is not observed in the spectrum of m-H-TiO₂, oxygen defects should locate in WO₃ rather than TiO₂. Based on previous reports, this is attributed to the higher structural stability of anatase TiO₂ against thermal reduction [49].

To further confirm the defective structure of WO₃, high-resolution XPS spectra of W 4f were measured (Fig. 2d). The doublet peaks centered at 35.5 eV (W1) and 37.6 eV (W2) are assigned to the characteristic 4f_{7/2} and 4f_{5/2} states of W⁶⁺, respectively [50]. Compared to m-WO₃, m-H-WO₃ exhibits two new peaks at 34.8 eV (W3) and 36.6 eV (W4), which can be attributed to the 4f_{7/2} and 4f_{5/2} states of W⁵⁺, respectively. The low valence of W confirms the introduction of oxygen vacancies and unpaired electrons into m-H-WO₃. The impact of oxygen vacancies on the electronic structure of WO₃ was thereafter examined by valance band (VB) XPS spectra. As shown in Fig. 2e, both m-WO₃ and m-H-WO₃ display similar band edges at ~2.40 eV, corresponding to the VB maximum of WO₃. For m-H-WO₃, it is evident that an additional electronic state emerges at 0.25 eV. This mid-gap state can be assigned to the localized electrons in the d-orbitals of low-valence W species, with enhanced electron migration and increased carrier density [51]. Compared to bare WO₃, m-H-WO₃/TiO₂ shows a smaller VB maximum value of 2.28 eV. This upward shift of band edge indicates a higher VB position of TiO₂ than WO₃, as schematically illustrated in Fig. 2f. Considering the larger band gap of TiO₂ than WO₃, the conduction band (CB) of TiO₂ would also locate at a

higher position than that of WO_3 . A type-II heterojunction can therefore form between WO_3 and TiO_2 , which is likely to provide a driving force for the charge separation. The photogenerated holes can migrate from WO_3 to TiO_2 for surface oxidation reactions, while the electrons would transfer in the opposite direction, thus achieving spatial separation of photocarriers. Moreover, the gap state located near the CB of WO_3 can act as an electron mediator and further accelerate the charge transfer process [52].

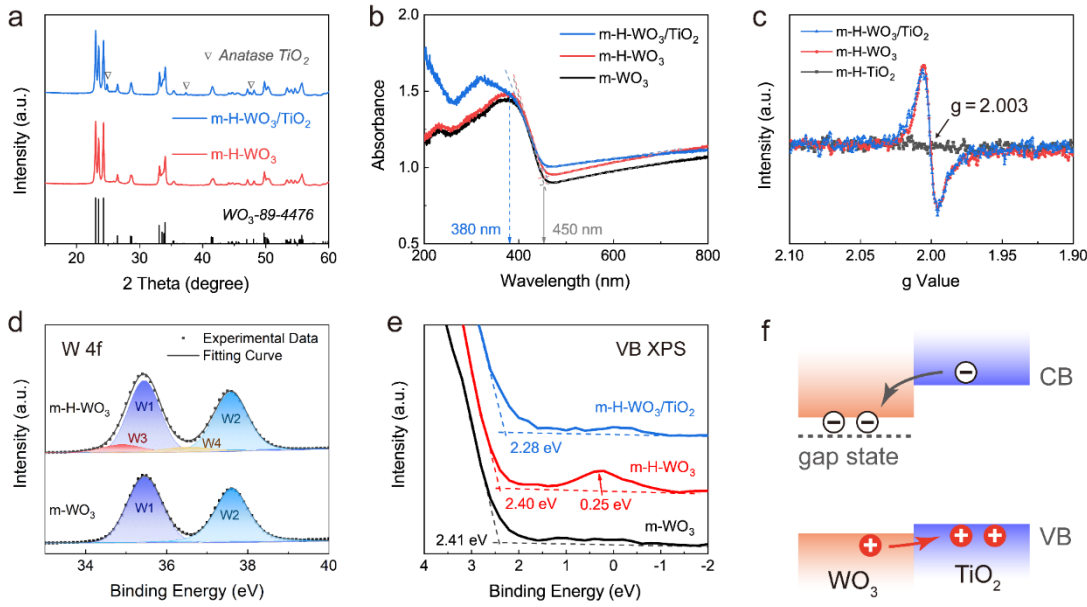


Fig. 2. (a) XRD patterns, (b) UV-visible absorption spectra, (c) ESR spectra, (d) W 4f XPS spectra, and (e) VB XPS spectra of different microfluidic photoelectrodes. (f) Schematic diagram of the band alignment between WO_3 and TiO_2 .

3.2. Charge separation behavior

The photoelectrochemical performance of microfluidic electrodes was evaluated using a standard three-electrode system under simulated solar irradiation (AM 1.5 G, 100 mW cm^{-2}). According to the chopped J-V curves in Fig. 3a, m- WO_3 photoanode achieves a photocurrent density of 0.8 mA cm^{-2} at 1.23 V vs. RHE, while the value for m-H- WO_3 is slightly higher. The formation of WO_3/TiO_2 heterointerface significantly improves the photoresponse of microfluidic photoanodes, together with the negatively shifted onset potential of 0.4 V vs. RHE for m- WO_3/TiO_2 . It is also worth noting that the introduction of oxygen defects into WO_3/TiO_2 heterostructure gives rise to a further increase in the photocurrent, reaching 1.3 mA cm^{-2} at 1.23 V vs. RHE for m-H- WO_3/TiO_2 . The much higher photocurrent density of m-H- WO_3/TiO_2 in comparison to m-H- WO_3 and m- WO_3/TiO_2 validates the synergistic effect between oxygen defects

1 and heterostructured interface for charge separation. The improved charge transfer
2 kinetics of interface-modulated nanojunction was further evaluated by EIS
3 measurements. Profiting from the good conductivity of carbon support, all the
4 microfluidic photoanodes possess low series resistance of less than $5\ \Omega$ (Fig. 3b). In the
5 Nyquist curves, m-H-WO₃/TiO₂ exhibits the smallest arc radius compared to the other
6 photoanodes, demonstrating the remarkably decreased charge transfer resistance. The
7 important contribution of oxygen defects to the photostability of microfluidic
8 photoanodes was thereafter evaluated by the time course of photocurrent, where both
9 m-WO₃ and m-WO₃/TiO₂ photoanodes experience obvious decrease in photocurrent
10 density during 1 h operation (Fig. 3c). XPS results indicate that one of the O 1s peaks
11 of m-WO₃ located at relatively high binding energy almost disappeared after the
12 polarization treatment (Fig. S6), which corresponds to the passivation of surface states.
13 We can therefore draw a conclusion that the PEC reactive sites of WO₃ are strongly
14 correlated with the surface oxygen-related defects [25,53]. Indeed, m-H-WO₃ and m-
15 H-WO₃/TiO₂ with massive surface defects show excellent photostability, further
16 indicating the pivotal contribution of interface modulation to the high performance of
17 microfluidic photoanodes. Furthermore, the wavelength-dependent incident photon to
18 current efficiency (IPCE) measurements of m-H-WO₃ and m-H-WO₃/TiO₂ were
19 conducted and displayed in Fig. 3d, where the enhancement factors contributed by TiO₂
20 were also calculated and shown. To circumvent the problem of different reaction
21 kinetics on WO₃ and TiO₂ surface, glycerol was added to the electrolyte to scavenge
22 holes. It can be observed that TiO₂ contributes to about 1.5-fold IPCE enhancement
23 factor in both UV and visible region, with the highest IPCE reaching nearly 75% for m-
24 H-WO₃/TiO₂. The excellent performance of TiO₂ decoration throughout the entire
25 photoresponse region suggests that the accelerated charge separation induced by TiO₂,
26 rather than the enhanced light absorption, may be the main reason for its high photon
27 utilization efficiency.

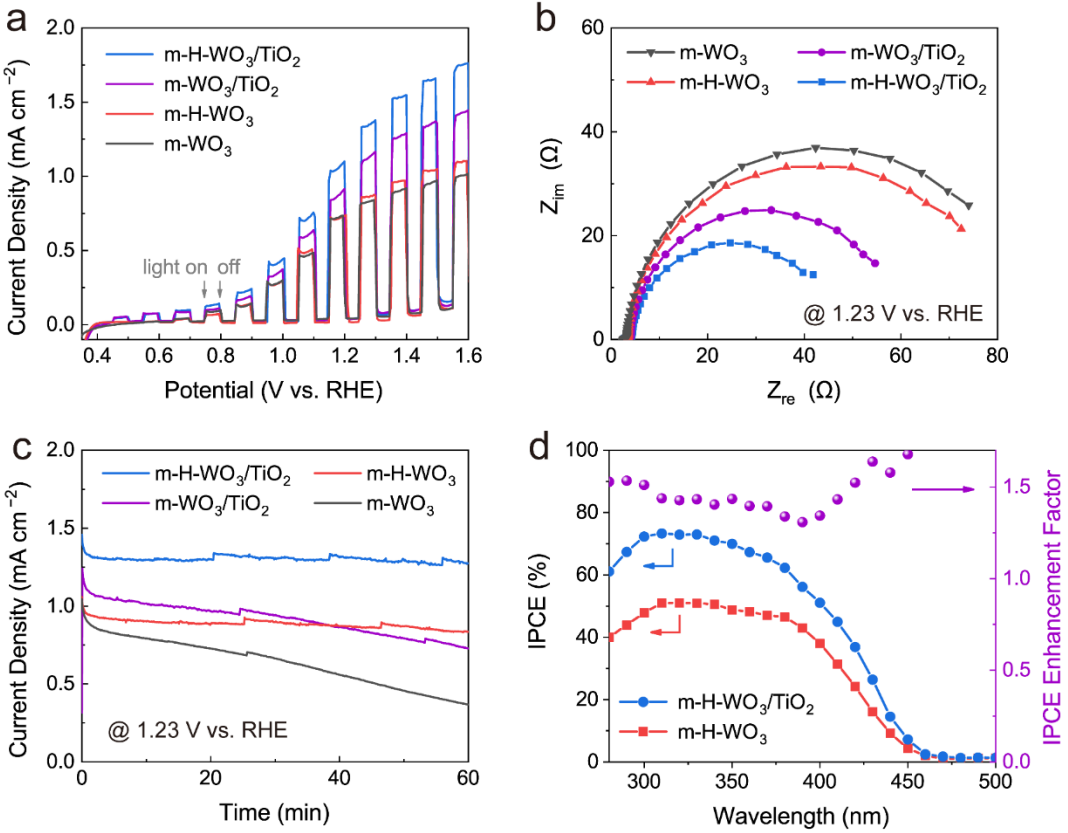


Fig. 3. (a) Chopped J–V curves, (b) EIS Nyquist plots, and (c) photocurrent-time curves of different microfluidic photoanodes. The electrolyte is 0.5 M Na₂SO₄ buffered by 0.1 M borate solution (pH = 6). The steps or abrupt increase appearing in the solid line in panel c are due to the abrupt burst of oxygen bubbles that formed and adhered to the Teflon electrode holder. (d) IPCE spectra of m-H-WO₃ and m-H-WO₃/TiO₂ measured at 1.23 V vs. RHE with the existence of 0.1 M glycerol.

To achieve a fundamental insight into the charge transfer process in the interface-modulated nanojunction, KPFM, a powerful tool to measure the surface potential with high spatial resolution, was utilized to visibly probe the charge separation at WO₃/TiO₂ interface. A model heterostructure, with anatase TiO₂ crystal deposited onto defective WO₃ microplate (H-WO₃), was assembled onto the graphite substrate (Fig. S7). This model structure with the WO₃/TiO₂ interface and oxygen defects exhibits enhanced PEC activity in a similar manner with the microfluidic photoanode, as demonstrated in Fig. S8. Therefore, it is reasonable to utilize this modeled photocatalyst to probe the spatial charge transfer and separation at the nanometer scale. By subtracting the surface potential measured under dark from that under light conditions (Fig. S9), we obtained the surface photovoltage (SPV) image of H-WO₃/TiO₂ heterojunction as depicted in

Fig. 4a. The representative cross-sectional SPV profiles associated with the dashed line in Fig. 4a are shown in Fig. 4b. It can be observed that TiO₂ and the major part of H-WO₃ show positive SPV signals of about 140 mV and 40 mV, respectively, indicating the presence of photogenerated holes on both H-WO₃ and TiO₂ [54]. The SPV value around the heterojunction interface decreases to 0 mV, which suggests the migration of electrons from TiO₂ to WO₃ and the accompanied holes migration from WO₃ to TiO₂ (Fig. 4b). In comparison, a much higher SPV value (60 mV) was observed in the interfacial region of WO₃/TiO₂ nanojunction without defect modulation (Fig. 4c and S10). Meanwhile, the SPV value of TiO₂ deposited on defect-free WO₃ was about 110 mV, which is much smaller than that on H-WO₃. The relative small potential difference across the WO₃/TiO₂ interface visually demonstrates its slow charge separation process. On the contrary, the charge separation on defective WO₃/TiO₂ nanojunction is faster, evidencing the important role of defects on interfacial charge transfer.

The unique feature of defective WO₃/TiO₂ interface was further confirmed by spatially resolved photoluminescence (PL) measurements using a similar model structure on glass, as the PL emission is directly associated with the electron-hole recombination [52,55]. Compared to the isolated one, junctional TiO₂ nanocrystal on defective WO₃ plate exhibits almost no fluorescence (Fig. 4d and S11), indicating the inhibited recombination of electrons and holes. In contrast, the integration of TiO₂ and defect-free WO₃ results in a negligible change in the fluorescence intensity (Fig. 4e). It can therefore be deduced that defect engineering can provide more opportunity for efficient charge separation in nanojunctions, which is in accordance with the KPFM results. As illustrated in Fig. 2f and 4f, WO₃ and TiO₂ form type-II heterostructure based on their energy band alignment, where the oxygen vacancies (V_O) in WO₃ introduce intraband state for charge reservation. The intraband V_O state with the fundamental role as an electron mediator can unambiguously enhance the charge separation in WO₃/TiO₂ nanojunction [52]. With accelerated electrons transfer from TiO₂ to H-WO₃, more photogenerated holes can accumulate on the surface of TiO₂, thereby speeding up the oxidation reaction (Fig. 4f).

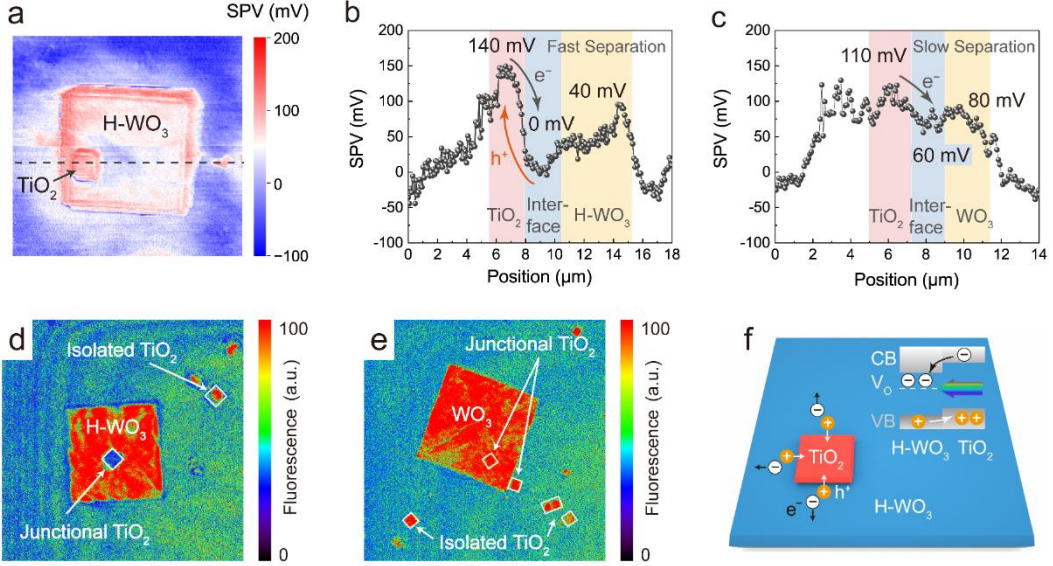


Fig. 4. (a) SPV image of H-WO₃/TiO₂ and (b) the representative cross-sectional SPV profiles associated with the dashed line in panel a. (c) The representative cross-sectional SPV profiles of defect-free WO₃/TiO₂ heterostructure. Spatially resolved PL images of (d) defective and (e) defect-free WO₃/TiO₂ heterostructure. (f) Schematic diagram of charge separation across the defective WO₃/TiO₂ interface. The energy band alignment and defect state induced by oxygen vacancies are also shown.

3.3. Flow field simulation

Apart from the photon utilization efficiency, the mass transfer of reactants on the photoelectrode surface is also of great significance. Therefore, the impact of microfluidic channels on the flow velocity and mass diffusion of reactants was investigated by computational fluid dynamics (CFD) simulation. A reaction box with the modeled structure in it was constructed, where the solution was allowed to pass through the catalyst with an initial velocity. For comparison, the planar structure with a liquid flow direction parallel to the electrode was also modeled and tested. Fig. 5 shows the liquid velocities of microfluidic and planar electrodes in the cross-sectional area, respectively. It can be observed that the spacings of carbon fibers provide unique microchannels for the liquid to flow through. As a consequence, the liquid flow rate near the catalyst surface is almost identical to that in the bulk, significantly compressing the diffusion layer and enabling the rapid diffusion of reactants and products in the microfluidic electrode (Fig. 5a) [41]. In contrast, the liquid velocity on the surface of planar electrode is almost zero, with an obvious laminar layer setting between the catalyst and bulk electrolyte (Fig. 5b). To have a closer look at the hydrodynamic

characteristics of planar electrode, a similar model with the inflow direction perpendicular to the electrode was constructed (Fig. S12). The planar electrode indeed acted as a physical barrier against the water flow and resulted in a 90° turn in the fluid direction. In this context, the outflow direction is always parallel to the planar electrode no matter what the inflow direction is, with a relatively low liquid velocity and limited mass transfer on the surface of planar electrode. The slow reactant diffusion would cause great restraint on the surface reaction, unavoidably leading to low hole utilization efficiency and overoxidation of organic molecules. This comparison indicates that the microfluidic architecture should possess fast reaction kinetics and high solar-to-chemical efficiency for PEC upgrading reactions.

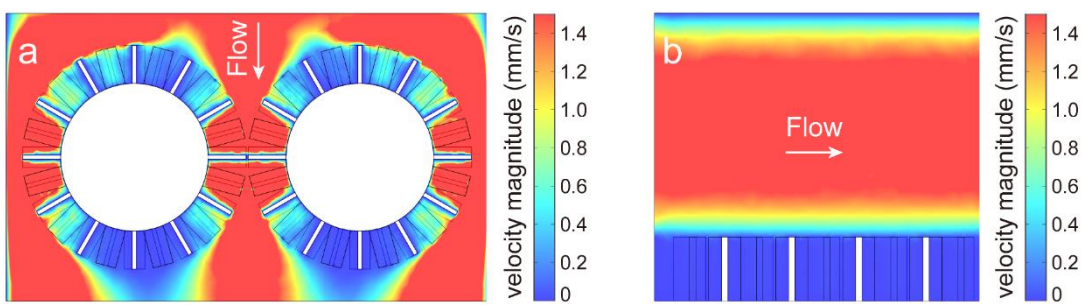


Fig. 5. CFD simulations of the flow velocity distribution in (a) microfluidic and (b) planar electrode.

3.4. PEC chemicals upgrading

Considering the fast reactants diffusion and nanojunction-enhanced hole accumulation on the surface of TiO₂, our 3-D hierarchical structure should be an ideal platform for PEC chemicals upgrading with high efficiency. To verify this hypothesis, microfluidic photoelectrodes were employed to upgrade glycerol into value-added fine chemicals [5]. For a reasonable comparison, planar WO₃ photoanodes with and without TiO₂ decoration were prepared on FTO conductive glass and referred to as pl-H-WO₃/TiO₂ and pl-H-WO₃, respectively. As a consequence of PEC oxidation, the addition of glycerol into the electrolyte solution leads to a significant increase of photoresponse (Fig. S13). The photocurrent density of m-H-WO₃/TiO₂ reaches 2.89 mA cm⁻² at 1.23 V vs. RHE, which is much higher than those of pl-H-WO₃ and pl-H-WO₃/TiO₂ (Fig. 6a). This well demonstrates the synergistic contribution of charge separation and mass transfer to the photon utilization in m-H-WO₃/TiO₂ photoanode. PEC glycerol oxidation was thereafter conducted at different applied potentials (0.6, 0.9, and 1.2 V vs. RHE) and the products were analyzed by HPLC and ¹H NMR methods (Fig. S14).

1 and S15). The glycerol consumption and product yields are listed in Table 1, with the
 2 generation rates of oxidation products on pl-H-WO₃ and m-H-WO₃/TiO₂ shown in Fig.
 3 6b. It can be concluded that the microfluidic photoanodes can efficiently convert
 4 glycerol into value-added glyceraldehyde (GLAD) and 1,3-dihydroxyacetone (DHA),
 5 with a small amount of formic acid (FA), glycolic acid (GA), and CO₂ as by-products.
 6 For m-H-WO₃/TiO₂ photoanode, the generation rate of valuable products (GLAD +
 7 DHA) reaches 35.3 μmol cm⁻² h⁻¹ at 1.2 V vs. RHE, with a selectivity of 85% (Fig. 6c)
 8 and faradaic efficiency (FE) of 70% (Fig. 6d). The production rate is about 3 times
 9 higher than that of conventional planar photoanode (pl-H-WO₃, 13.3 μmol cm⁻² h⁻¹).
 10 Meanwhile, the selectivity and faradaic efficiency of pl-H-WO₃ toward (GLAD + DHA)
 11 generation are 61% and 42% at 1.2 V vs. RHE, respectively, which are much smaller
 12 than those of m-H-WO₃/TiO₂. Profited from the enhanced diffusion of glycerol
 13 molecules and their oxidation derivatives in microflow channels, the microfluidic
 14 platform not only exhibits exceedingly high activity over the entire range of potentials
 15 (0.6–1.2 V vs. RHE), but also inhibits the overoxidation of glycerol into by-products
 16 such as formic acid and glycolic acid (entry 1–6 in Table 1 and Fig. 6b–d) [56]. It should
 17 also be noted that CO₂, the complete oxidation product of glycerol, only accounts for
 18 less than 6% of the total carbonaceous products in the microfluidic systems, while those
 19 values for the planar systems are about 20% (Table 1). No difference in product
 20 compositions is observed for m-H-WO₃ and m-H-WO₃/TiO₂. Thus, the type of
 21 semiconductors presents little impact on the reaction selectivity. Finally, to rule out the
 22 possible generation of toxic compounds, cytotoxicity tests were conducted on the
 23 glycerol solutions before and after PEC oxidation on m-H-WO₃/TiO₂. The glycerol
 24 sample after PEC oxidation showed a promoting effect on the cell viability (Fig. S16),
 25 demonstrating that the oxidation products of glycerol are rather nutrient than toxicant.
 26 All these results demonstrate the inherent advantages of microfluidic platform,
 27 contributing to the state-of-the-art PEC performance of m-H-WO₃/TiO₂ photoanode for
 28 glycerol upgrading [56–58].

29 **Table 1** PEC glycerol consumption and product yields on different photoanodes

| Entry | Photoanode | Potential | | Glycerol Consumption [μmol] | Products [μmol] | | | | Carbon Balance | CO ₂ Yield |
|-------|---------------------------------------|-------------|------------|-----------------------------|-----------------|-----|-----|-----|----------------|-----------------------|
| | | [V vs. RHE] | Charge [C] | | GLAD | DHA | FA | GA | | |
| 1 | m-H-WO ₃ /TiO ₂ | 0.6 | 10.2 | 44.4 | 29.1 | 9.9 | 2.7 | 1.2 | 6.5 | 96.5% 4.9% |

| | | | | | | | | | | | |
|----|--|-----|------|-------|------|------|------|-----|------|-------|-------|
| 2 | m-H-WO ₃ /TiO ₂ | 0.9 | 21.2 | 93.0 | 59.4 | 20.1 | 5.7 | 2.7 | 13.2 | 94.2% | 4.7% |
| 3 | m-H-WO ₃ /TiO ₂ | 1.2 | 29.2 | 123.6 | 77.7 | 28.2 | 7.2 | 3.3 | 21.7 | 95.3% | 5.9% |
| 4 | m-H-WO ₃ | 0.6 | 4.1 | 18.3 | 12.0 | 4.2 | 1.2 | 0.3 | 3.3 | 97.8% | 6.0% |
| 5 | m-H-WO ₃ | 0.9 | 12.4 | 54.9 | 34.8 | 12.3 | 3.3 | 1.8 | 6.8 | 94.1% | 4.1% |
| 6 | m-H-WO ₃ | 1.2 | 17.5 | 75.9 | 50.1 | 15.9 | 4.8 | 2.4 | 8.4 | 94.9% | 3.7% |
| 7 | pl-H-WO ₃ /TiO ₂ | 0.6 | 7.3 | 25.5 | 12.6 | 4.8 | 5.4 | 2.7 | 10.8 | 96.5% | 14.1% |
| 8 | pl-H-WO ₃ /TiO ₂ | 0.9 | 15.3 | 54.6 | 25.2 | 9.0 | 11.4 | 5.4 | 33.4 | 96.6% | 20.4% |
| 9 | pl-H-WO ₃ /TiO ₂ | 1.2 | 24.2 | 81.6 | 36.3 | 12.9 | 12.6 | 6.0 | 53.5 | 92.2% | 21.9% |
| 10 | pl-H-WO ₃ | 0.6 | 4.5 | 18.9 | 9.5 | 3.2 | 3.7 | 1.8 | 8.9 | 95.8% | 15.7% |
| 11 | pl-H-WO ₃ | 0.9 | 13.3 | 51.2 | 23.1 | 8.7 | 9.8 | 4.5 | 30.2 | 94.0% | 19.7% |
| 12 | pl-H-WO ₃ | 1.2 | 18.1 | 65.4 | 29.6 | 10.4 | 10.7 | 5.3 | 45.6 | 95.3% | 23.2% |

1 Reaction conditions: 20 mL 0.5 M Na₂SO₄, 0.1 M borate buffer, and 0.1 M glycerol,
 2 pH = 6, electrode area = 3 cm², 30°C.

3 We then employed cyclohexane and HSO₄⁻ as the representative hydrocarbon and
 4 inorganic substrates to verify the versatility of this microfluidic PEC electrode.
 5 Selective oxidation of cyclohexane is intrinsically important in the chemistry of C-H
 6 activation and the commercial synthesis of Nylon [59]. As shown in Fig. 6e, m-H-
 7 WO₃/TiO₂ photoanode can efficiently and selectively transform cyclohexane into
 8 value-added KA oil (cyclohexanol and cyclohexanone). The yield of KA oil on m-H-
 9 WO₃/TiO₂ reaches 64 μmol cm⁻² after 5 h reaction, which is nearly 2 times higher than
 10 that of pl-H-WO₃. Benefiting from the numerous reaction sites, m-H-WO₃/TiO₂
 11 maintains a relatively high faradaic efficiency in comparison to its planar counterpart
 12 (Fig. S17). Similar results can be observed for the oxidation of HSO₄⁻ to S₂O₈²⁻, where
 13 99% faradaic efficiency can be realized by m-H-WO₃/TiO₂ in the first 20 minutes of
 14 oxidation (Fig. 6f and S17). As a strong oxidant, S₂O₈²⁻ is of great value and widely
 15 used for many chemical and environmental reactions [9]. About 4 mM S₂O₈²⁻ can be
 16 obtained by m-H-WO₃/TiO₂ after PEC oxidation for 2 hours, which is much higher than
 17 that of pl-H-WO₃ (2.4 mM) (Fig. 6f). In this context, the nanojunction-enhanced
 18 microfluidic PEC platform offers more opportunity for PEC oxidative upgrading of
 19 various chemicals.

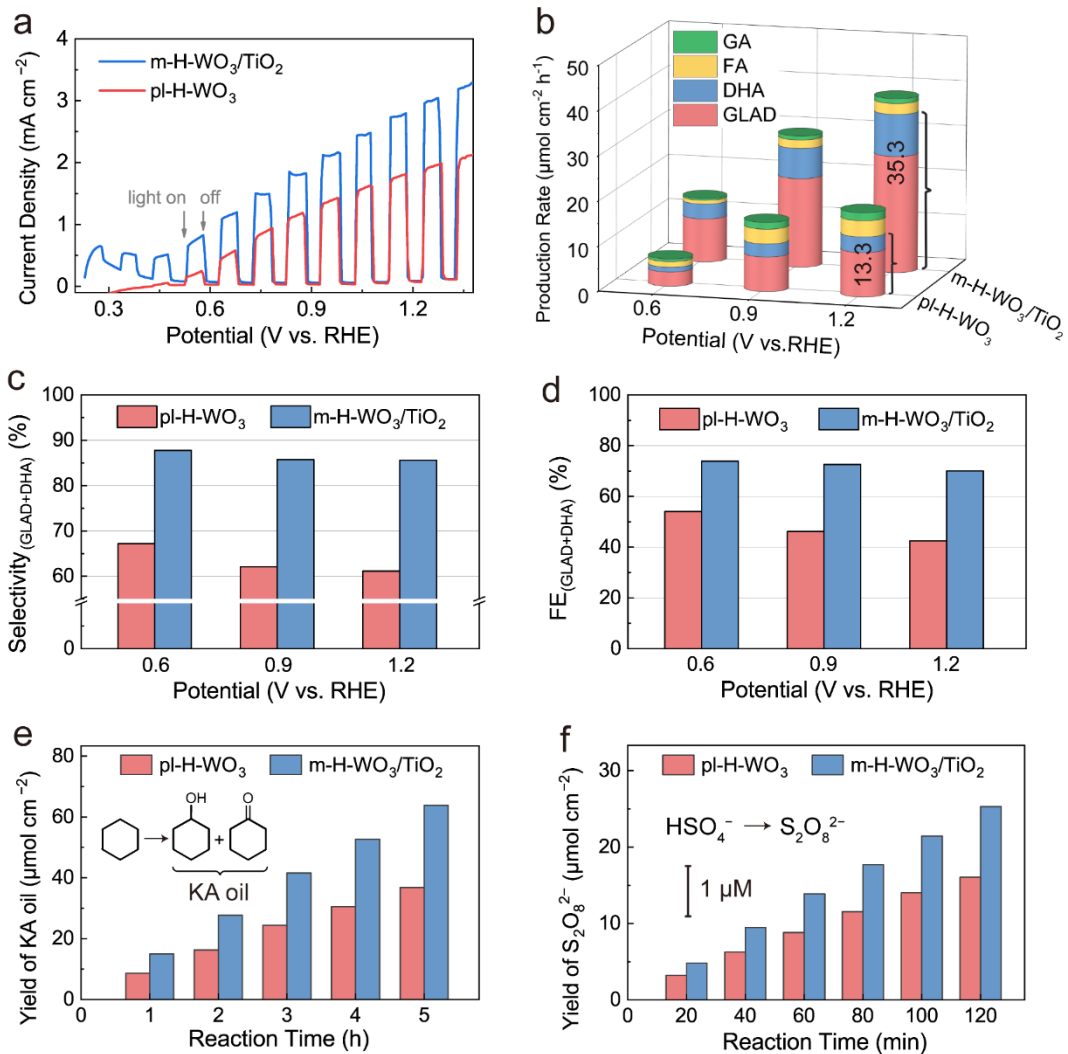


Fig. 6. (a) Chopped J–V curves of pl-H-WO₃ and m-H-WO₃/TiO₂ photoanodes. (b) PEC production rates of glycerol oxidative products. (c) Selectivities and (d) faradaic efficiencies of pl-H-WO₃ and m-H-WO₃/TiO₂ for the production of valuable products (GLAD + DHA). The electrolyte for panel a–d is a mixture of 0.5 M Na₂SO₄, 0.1 M glycerol, and 0.1 M borate buffer (pH = 6). (e) Generation of KA oil in the PEC oxidation of cyclohexane. Electrolysis was conducted at 0.8 V vs. Ag/Ag⁺. The electrolyte was a mixture of 18 mL cyclohexane, 12 mL t-BuOH, and 2 mL HNO₃. (f) Generation of S₂O₈²⁻ in the PEC oxidation of HSO₄⁻. Electrolysis was conducted at 1.2 V vs. RHE in 20 mL 0.5 M H₂SO₄ solution.

3.5. PEC pollutants degradation

With numerous flow channels and oxidation sites, m-H-WO₃/TiO₂ should also be a good candidate for the PEC degradation of organic pollutants. Bisphenol A (BPA), a representative environmental contaminant with adverse effects on endocrine systems of human and aquatic organisms, was used to evaluate the potential of this microfluidic

photoanode for pollutant removal. Before photoelectrocatalytic degradation, the photoanodes were immersed into BPA solution for 60 min under dark conditions to reach the adsorption-desorption equilibrium. Compared to planar electrodes, the adsorption capacities of BPA on microfluidic electrodes are much higher, verifying their ample reaction sites (Fig. 7a). Upon illumination, more than 99% of BPA was decomposed over m-H-WO₃/TiO₂ after 90 min, while the degradation efficiency of pl-H-WO₃ was only 67%. Both TiO₂ decoration and construction of microflow channels contribute to the fast BPA elimination, with the BPA degradation efficiencies of pl-H-WO₃/TiO₂ and m-H-WO₃ being 81% and 98%, respectively. It can be therefore deduced that in comparison to charge separation on photoanode, the mass transfer of BPA is more important for its fast PEC degradation. To have a quantitative analysis on BPA degradation process, pseudo-first-order kinetics was employed to simulate all the PEC degradation plots (Fig. 7b). It can be observed that m-H-WO₃/TiO₂ exhibits an apparent rate constant (k) of 0.060 min⁻¹ for BPA degradation, which is 5-fold higher than that of pl-H-WO₃ (0.012 min⁻¹). Furthermore, the rate constant of m-H-WO₃ (0.039 min⁻¹) is relatively higher than that of pl-H-WO₃/TiO₂ (0.018 min⁻¹). This proves the significant contribution of mass transfer in microflow channels to the fast PEC degradation. The decolorization of methylene blue (MB) was also tested to investigate the versatility of m-H-WO₃/TiO₂ photoanode. As shown in Fig. 7c, the solution was totally decolorized over m-H-WO₃/TiO₂ after 90 min, with nearly 5-fold higher reaction kinetics ($k = 0.064 \text{ min}^{-1}$) than pl-H-WO₃ ($k = 0.014 \text{ min}^{-1}$). The extraordinary performance of microfluidic photoanode in BPA and MB elimination suggests its potential applicability for environmental remediation. More importantly, m-H-WO₃/TiO₂ shows a negligible decrease of activity during five cycling runs, indicating its good photostability (Fig. 7d). In this regard, the nanojunction-enhanced microfluidic PEC platform demonstrates great potential for the fast elimination of various aquatic pollutants.

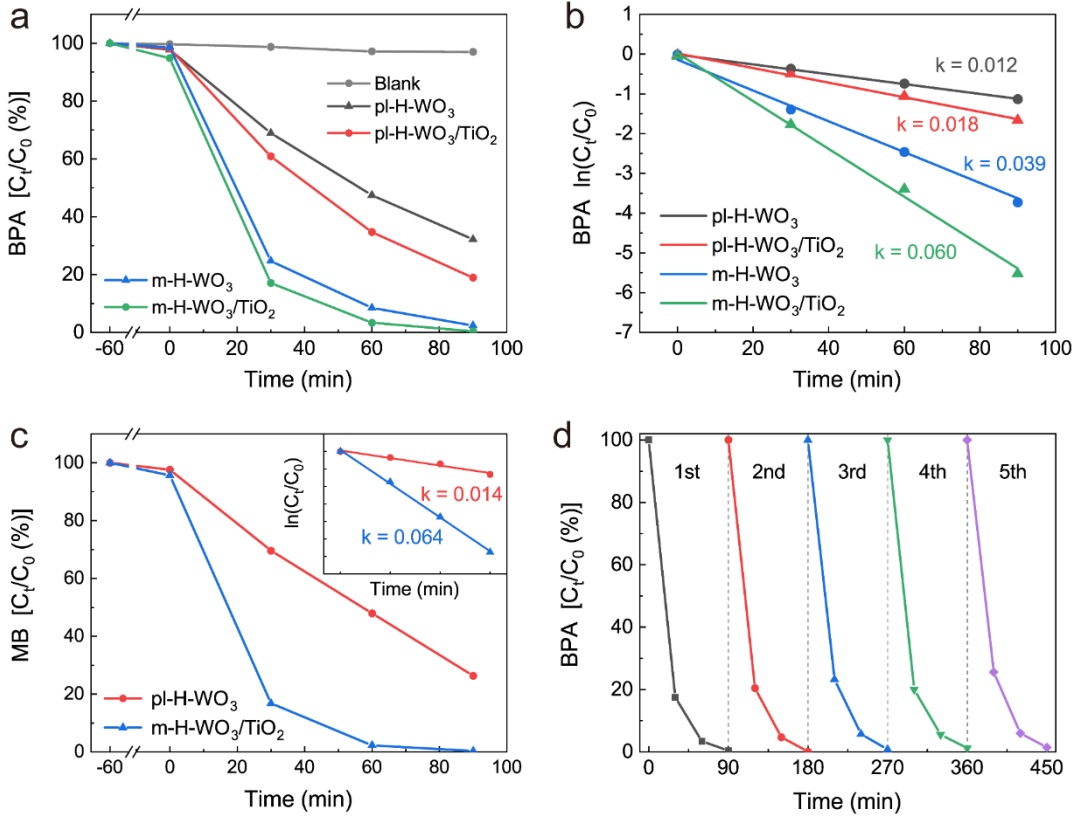
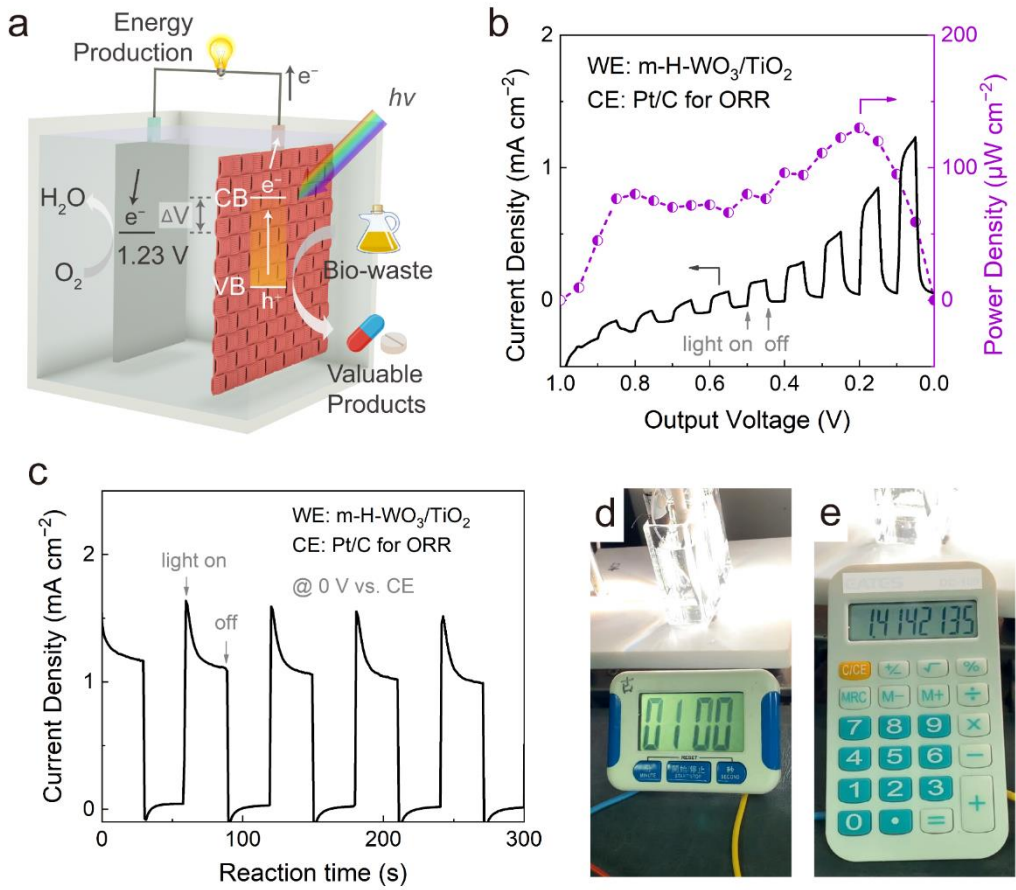


Fig. 7. (a) PEC degradation of BPA and (b) the corresponding kinetics plots over different photoanodes. (c) PEC degradation of MB and the corresponding kinetics plots. (d) Cycling degradation of BPA over m-H-WO₃/TiO₂. The degradation experiments were conducted at 1 V vs. RHE in 0.1 M Na₂SO₄ solution containing 10 mg L⁻¹ pollutants (pH = 6) under simulated solar-light irradiation (AM 1.5 G, 100 mW cm⁻²).

3.6. Photocatalytic fuel cell

Having demonstrated the extraordinary performance of microfluidic photoanode for oxidative chemicals upgrading, we attempted to design a bias-free PEC system for self-sustained organic synthesis. As illustrated in Fig. 8a, a two-electrode photocatalytic fuel cell (PFC) was constructed by using m-H-WO₃/TiO₂ as the photoanode and Pt/C coated carbon paper as the cathode for oxygen reduction reaction (ORR) [60]. When glycerol is employed as the organic source, an open-circuit potential of 0.9 V and a short-circuit current of 1.2 mA cm⁻² are realized using such an integrated device (Fig. 8b). Correspondingly, a maximum output power density of 130 μW cm⁻² is obtained, which is among the highest values reported to date (Table S1). Besides, this photocatalytic fuel cell can maintain a stable current of ~1.2 mA cm⁻² at 0 V vs. CE (i.e. without external electric bias), demonstrating its good stability for electricity generation (Fig.

1 8c). By connecting two of above photocatalytic fuel cells in series, a higher output
 2 voltage can be easily realized, which is sufficient to power common electronic devices
 3 with the nominal voltage of 1.5 V, such as electronic timer (Fig. 8d and Video S1) and
 4 calculator (Fig. 8e and Video S2). The above results demonstrate that we can
 5 simultaneously obtain value-added chemicals and electricity by this PFC system.



6
 7 **Fig. 8.** (a) Schematic diagram of the PFC system with microfluidic photoanode and
 8 ORR cathode. (b) Chopped J–V curve of the PFC system. The output power density is
 9 also shown and calculated by multiplying the photocurrent density by the output voltage.
 10 (c) Chopped photocurrent-time profiles of the PFC system at short circuit. Photographs
 11 showing (d) an electronic timer and (e) an electronic calculator powered by two of the
 12 PFC cells connected in series.

13 4. Conclusion

14 In conclusion, we demonstrated an efficient photoelectrochemical platform based on
 15 WO₃/TiO₂ nanojunction with engineered defects and microfluidic structure. Profiting
 16 from the nanojunction-enhanced charge separation and microchannel-facilitated mass
 17 transfer, this 3-D nanoarchitecture exhibited unprecedented activity and selectivity for

1 chemical upgrading of various organic and inorganic compounds. The impressive
2 production rates of high value-added chemicals by glycerol oxidation ($35.3 \mu\text{mol cm}^{-2}$
3 h^{-1}) and cyclohexane activation ($12.8 \mu\text{mol cm}^{-2} \text{h}^{-1}$) were nearly 3 and 2 times higher
4 than those of conventional planar system. The interface-modulated photoanode also
5 contributed to 5-fold higher degradation kinetics for the removal of two representative
6 organic pollutants (BPA and MB). A highly efficient photocatalytic fuel cell with high
7 open-circuit potential (0.9 V) and short-circuit current (1.2 mA cm^{-2}) was finally
8 constructed based on this nanojunction-enhanced microfluidic photoanode. We thus
9 can simultaneously obtain value-added chemicals and electricity by this two-in-one
10 photocatalytic fuel cell system. Thus, this work not only provides an inspiring approach
11 to visualize the charge separation in heterostructured architectures, but also
12 demonstrates the great potential of microfluidic PEC system for solar energy utilization
13 toward a sustainable and low-carbon society.

14 **Acknowledgments**

15 This work was financially supported by the National Natural Science Foundation of
16 China (No. 51978372 and 51538013) and the National Key R&D Program of China
17 (Grant No. 2019YFA0705802). The authors would like to thank Prof. Aijie Wang for
18 her help in glycerol oxidation products analysis. We also thank Dr. William A. Jefferson
19 for proofreading this manuscript.

20 **Supplementary data**

21 Experimental procedures, SEM and TEM images, O 1s XPS spectra, KPFM results,
22 spatially resolved photoluminescence image, identification of reaction products,
23 faradaic efficiencies for the production of KA oil and $\text{S}_2\text{O}_8^{2-}$, cytotoxicity results,
24 performance comparison of photocatalytic fuel cells.

25 Assembly of two photocatalytic fuel cells to power common electric devices (Videos).

26 **References**

- 27 [1] M. Wang, J. Ma, H. Liu, N. Luo, Z. Zhao, F. Wang, Sustainable productions of
28 organic acids and their derivatives from biomass via selective oxidative cleavage of
29 C–C bond, ACS Catal., 8 (2018) 2129-2165.
- 30 [2] L. Chen, J. Tang, L.-N. Song, P. Chen, J. He, C.-T. Au, S.-F. Yin, Heterogeneous
31 photocatalysis for selective oxidation of alcohols and hydrocarbons, Appl. Catal. B
32 Environ., 242 (2019) 379-388.

- [3] G. Dodekatos, S. Schünemann, H. Tüysüz, Recent advances in thermo-, photo-, and electrocatalytic glycerol oxidation, *ACS Catal.*, 8 (2018) 6301-6333.
- [4] M. Simões, S. Baranton, C. Coutanceau, Electrochemical valorisation of glycerol, *ChemSusChem*, 5 (2012) 2106-2124.
- [5] D. Liu, J.-C. Liu, W. Cai, J. Ma, H.B. Yang, H. Xiao, J. Li, Y. Xiong, Y. Huang, B. Liu, Selective photoelectrochemical oxidation of glycerol to high value-added dihydroxyacetone, *Nat. Commun.*, 10 (2019) 1779.
- [6] J. Zou, Z. Wang, W. Guo, B. Guo, Y. Yu, L. Wu, Photocatalytic selective oxidation of benzyl alcohol over ZnTi-LDH: The effect of surface OH groups, *Appl. Catal. B Environ.*, 260 (2020) 118185.
- [7] P. Zhang, X. Sheng, X. Chen, Z. Fang, J. Jiang, M. Wang, F. Li, L. Fan, Y. Ren, B. Zhang, B.J.J. Timmer, M.S.G. Ahlquist, L. Sun, Paired electrocatalytic oxygenation and hydrogenation of organic substrates with water as the oxygen and hydrogen source, *Angew. Chem. Int. Ed.*, 58 (2019) 9155-9159.
- [8] J. Xie, R. Jin, A. Li, Y. Bi, Q. Ruan, Y. Deng, Y. Zhang, S. Yao, G. Sankar, D. Ma, J. Tang, Highly selective oxidation of methane to methanol at ambient conditions by titanium dioxide-supported iron species, *Nat. Catal.*, 1 (2018) 889-896.
- [9] K. Sayama, Production of high-value-added chemicals on oxide semiconductor photoanodes under visible light for solar chemical-conversion processes, *ACS Energy Lett.*, 3 (2018) 1093-1101.
- [10] Y. Sun, X. Li, J. Wang, W. Ning, J. Fu, X. Lu, Z. Hou, Carbon film encapsulated Pt NPs for selective oxidation of alcohols in acidic aqueous solution, *Appl. Catal. B Environ.*, 218 (2017) 538-544.
- [11] X. Dai, S. Adomeit, J. Rabeh, C. Kreyenschulte, A. Brückner, H. Wang, F. Shi, Sustainable co-synthesis of glycolic acid, formamides and formates from 1,3-dihydroxyacetone by a Cu/Al₂O₃ catalyst with a single active sites, *Angew. Chem. Int. Ed.*, 58 (2019) 5251-5255.
- [12] S. Cattaneo, M. Stucchi, A. Villa, L. Prati, Gold Catalysts for the selective oxidation of biomass-derived products, *ChemCatChem*, 11 (2019) 309-323.
- [13] F. Li, Y. Wang, J. Du, Y. Zhu, C. Xu, L. Sun, Simultaneous oxidation of alcohols and hydrogen evolution in a hybrid system under visible light irradiation, *Appl. Catal. B Environ.*, 225 (2018) 258-263.

- [14] S. Zhao, Z. Dai, W. Guo, F. Chen, Y. Liu, R. Chen, Highly selective oxidation of glycerol over Bi/Bi_{3.64}Mo_{0.36}O_{6.55} heterostructure: Dual reaction pathways induced by photogenerated ¹O₂ and holes, *Appl. Catal. B Environ.*, 244 (2019) 206-214.
- [15] A. Savateev, I. Ghosh, B. König, M. Antonietti, Photoredox catalytic organic transformations using heterogeneous carbon nitrides, *Angew. Chem. Int. Ed.*, 57 (2018) 15936-15947.
- [16] L. Luo, Z.-j. Wang, X. Xiang, D. Yan, J. Ye, Selective activation of benzyl alcohol coupled with photoelectrochemical water oxidation via a radical relay strategy, *ACS Catal.*, 10 (2020) 4906-4913.
- [17] S. Wu, X. Tan, J. Lei, H. Chen, L. Wang, J. Zhang, Ga-doped and Pt-loaded porous TiO₂-SiO₂ for photocatalytic nonoxidative coupling of methane, *J. Am. Chem. Soc.*, 141 (2019) 6592-6600.
- [18] J. Xie, S.A. Shevlin, Q. Ruan, S.J.A. Moniz, Y. Liu, X. Liu, Y. Li, C.C. Lau, Z.X. Guo, J. Tang, Efficient visible light-driven water oxidation and proton reduction by an ordered covalent triazine-based framework, *Energy Environ. Sci.*, 11 (2018) 1617-1624.
- [19] Y. Li, Z. Liu, M. Ruan, Z. Guo, X. Li, 1D WO₃ nanorods/2D WO_{3-x} nanoflakes homojunction structure for enhanced charge separation and transfer towards efficient photoelectrochemical performance, *ChemSusChem*, 12 (2019) 5282-5290.
- [20] Y. Li, Z. Liu, J. Li, M. Ruan, Z. Guo, An effective strategy of constructing a multi-junction structure by integrating a heterojunction and a homojunction to promote the charge separation and transfer efficiency of WO₃, *J. Mater. Chem. A*, 8 (2020) 6256-6267.
- [21] Q. Niu, X. Gu, L. Li, Y. Zhang, G. Zhao, 3D CQDs-{001}TiO₂/Ti photoelectrode with dominant {001} facets: Efficient visible-light-driven photoelectrocatalytic oxidation of organic pollutants and mechanism insight, *Appl. Catal. B Environ.*, 261 (2020) 118229.
- [22] S. Han, Q. Niu, N. Qin, X. Gu, Y. Zhang, G. Zhao, In situ growth of M-{001}TiO₂/Ti photoelectrodes: synergistic dominant {001} facets and ratio-optimal surface junctions for the effective oxidation of environmental pollutants, *Chem. Commun.*, 56 (2020) 1337-1340.
- [23] T. Wang, W. Yin, X. Yu, X. An, A strategy of enhancing photoactivity of TiO₂ via facet-dependent pyrolysis of dicyandiamide, *Appl. Catal. B Environ.*, 264 (2020) 118527.

- [24] Q. Tang, X. An, H. Lan, H. Liu, J. Qu, Polyoxometalates/TiO₂ photocatalysts with engineered facets for enhanced degradation of bisphenol A through persulfate activation, *Appl. Catal. B Environ.*, 268 (2020) 118394.
- [25] Z. Gu, L. Zhang, B. Wen, X. An, H. Lan, L.-M. Liu, T. Chen, J. Zhang, X. Cao, J. Tang, H. Liu, J. Qu, Efficient design principle for interfacial charge separation in hydrogen-intercalated nonstoichiometric oxides, *Nano Energy*, 53 (2018) 887-897.
- [26] X. An, L. Zhang, B. Wen, Z. Gu, L.-M. Liu, J. Qu, H. Liu, Boosting photoelectrochemical activities of heterostructured photoanodes through interfacial modulation of oxygen vacancies, *Nano Energy*, 35 (2017) 290-298.
- [27] S. Zhang, Z. Liu, D. Chen, Z. Guo, M. Ruan, Oxygen vacancies engineering in TiO₂ homojunction/ZnFe-LDH for enhanced photoelectrochemical water oxidation, *Chem. Eng. J.*, 395 (2020) 125101.
- [28] S. Meng, W. Sun, S. Zhang, X. Zheng, X. Fu, S. Chen, Insight into the transfer mechanism of photogenerated carriers for WO₃/TiO₂ heterojunction photocatalysts: Is it the transfer of band–band or Z-scheme? Why?, *J. Phys. Chem. C*, 122 (2018) 26326-26336.
- [29] Q. Zeng, J. Bai, J. Li, B. Zhou, Y. Sun, A low-cost photoelectrochemical tandem cell for highly-stable and efficient solar water splitting, *Nano Energy*, 41 (2017) 225-232.
- [30] X. Shen, F. Xiao, H. Zhao, Y. Chen, C. Fang, R. Xiao, W. Chu, G. Zhao, In situ-formed PdFe nanoalloy and carbon defects in cathode for synergic reduction–oxidation of chlorinated pollutants in electro-Fenton process, *Environ. Sci. Technol.*, 54 (2020) 4564-4572.
- [31] B. Niu, J. Cai, W. Song, G. Zhao, Novel electrochemical pretreatment for preferential removal of nonylphenol in industrial wastewater: Biodegradability improvement and toxicity reduction, *Environ. Sci. Technol.*, 54 (2020) 1258-1266.
- [32] R. Mazzaro, S. Boscolo Bibi, M. Natali, G. Bergamini, V. Morandi, P. Ceroni, A. Vomiero, Hematite nanostructures: An old material for a new story. Simultaneous photoelectrochemical oxidation of benzylamine and hydrogen production through Ti doping, *Nano Energy*, 61 (2019) 36-46.
- [33] J. Zhang, B. Tang, Z. Zhu, G. Zhao, Size-controlled microporous SiO₂ coated TiO₂ nanotube arrays for preferential photoelectrocatalytic oxidation of highly toxic PAEs, *Appl. Catal. B Environ.*, 268 (2020) 118400.

- 1 [34] S. Xiao, Z. Wan, J. Zhou, H. Li, H. Zhang, C. Su, W. Chen, G. Li, D. Zhang, H.
2 Li, Gas-phase photoelectrocatalysis for breaking down nitric oxide, Environ. Sci.
3 Technol., 53 (2019) 7145-7154.
- 4 [35] H. Li, S. Xiao, J. Zhou, J. Zhao, F. Liu, G. Li, D. Zhang, A flexible CdS nanorods-
5 carbon nanotubes/stainless steel mesh photoanode for boosted photoelectrocatalytic
6 hydrogen evolution, Chem. Commun., 55 (2019) 2741-2744.
- 7 [36] V. Nair, J.C. Colmenares, D. Lisoviytskiy, Ultrasound assisted ZnO coating in a
8 microflow based photoreactor for selective oxidation of benzyl alcohol to
9 benzaldehyde, Green Chem., 21 (2019) 1241-1246.
- 10 [37] H. Yan, Z.-W. Hou, H.-C. Xu, Photoelectrochemical C–H alkylation of
11 heteroarenes with organotrifluoroborates, Angew. Chem. Int. Ed., 58 (2019) 4592-
12 4595.
- 13 [38] F. Parrino, M. Bellardita, E.I. García-López, G. Marcì, V. Loddo, L. Palmisano,
14 Heterogeneous photocatalysis for selective formation of high-value-added
15 molecules: Some chemical and engineering aspects, ACS Catal., 8 (2018) 11191-
16 11225.
- 17 [39] Y. Huang, Z. Guo, H. Liu, S. Zhang, P. Wang, J. Lu, Y. Tong, Heterojunction
18 architecture of N-doped WO₃ nanobundles with Ce₂S₃ nanodots hybridized on a
19 carbon textile enables a highly efficient flexible photocatalyst, Adv. Funct. Mater.,
20 29 (2019) 1903490.
- 21 [40] Z. Gu, X. An, H. Lan, Y. Tian, J. Zhang, R. Liu, H. Liu, J. Qu, Microfluidic-
22 enhanced 3-D photoanodes with free interfacial energy barrier for
23 photoelectrochemical applications, Appl. Catal. B Environ., 244 (2019) 740-747.
- 24 [41] P. He, X. Tang, L. Chen, P. Xie, L. He, H. Zhou, D. Zhang, T. Fan, Patterned
25 carbon nitride–based hybrid aerogel membranes via 3D printing for broadband solar
26 wastewater remediation, Adv. Funct. Mater., 28 (2018) 1801121.
- 27 [42] D. Cambié, C. Bottecchia, N.J.W. Straathof, V. Hessel, T. Noël, Applications of
28 continuous-flow photochemistry in organic synthesis, material science, and water
29 treatment, Chem Rev, 116 (2016) 10276-10341.
- 30 [43] Y. Sheng, H. Miao, J. Jing, W. Yao, Y. Zhu, Perylene diimide anchored graphene
31 3D structure via π - π interaction for enhanced photoelectrochemical degradation
32 performances, Appl. Catal. B Environ., 272 (2020) 118897.

- 1 [44] Y. Wang, W. Tian, C. Chen, W. Xu, L. Li, Tungsten trioxide nanostructures for
2 photoelectrochemical water splitting: Material engineering and charge carrier
3 dynamic manipulation, *Adv. Funct. Mater.*, 29 (2019) 1809036.
- 4 [45] S. Wang, H. Chen, G. Gao, T. Butburee, M. Lyu, S. Thaweesak, J.H. Yun, A. Du,
5 G. Liu, L. Wang, Synergistic crystal facet engineering and structural control of WO_3
6 films exhibiting unprecedented photoelectrochemical performance, *Nano Energy*,
7 24 (2016) 94-102.
- 8 [46] H.G. Yang, C.H. Sun, S.Z. Qiao, J. Zou, G. Liu, S.C. Smith, H.M. Cheng, G.Q.
9 Lu, Anatase TiO_2 single crystals with a large percentage of reactive facets, *Nature*,
10 453 (2008) 638-641.
- 11 [47] R. Chen, S. Pang, H. An, J. Zhu, S. Ye, Y. Gao, F. Fan, C. Li, Charge separation
12 via asymmetric illumination in photocatalytic Cu_2O particles, *Nat. Energy*, 3 (2018)
13 655-663.
- 14 [48] T. Wei, Y.-N. Zhu, X. An, L.-M. Liu, X. Cao, H. Liu, J. Qu, Defect modulation of
15 Z-Scheme $\text{TiO}_2/\text{Cu}_2\text{O}$ photocatalysts for durable water splitting, *ACS Catal.*, 9
16 (2019) 8346-8354.
- 17 [49] W. Huang, J. Wang, L. Bian, C. Zhao, D. Liu, C. Guo, B. Yang, W. Cao, Oxygen
18 vacancy induces self-doping effect and metalloid LSPR in non-stoichiometric
19 tungsten suboxide synergistically contributing to the enhanced
20 photoelectrocatalytic performance of $\text{WO}_{3-x}/\text{TiO}_{2-x}$ heterojunction, *Phys Chem
Chem Phys*, 20 (2018) 17268-17278.
- 22 [50] D. Liu, C. Wang, Y. Yu, B.-H. Zhao, W. Wang, Y. Du, B. Zhang, Understanding
23 the nature of ammonia treatment to synthesize oxygen vacancy-enriched transition
24 metal oxides, *Chem*, 5 (2019) 376-389.
- 25 [51] N. Zhang, A. Jalil, D. Wu, S. Chen, Y. Liu, C. Gao, W. Ye, Z. Qi, H. Ju, C. Wang,
26 X. Wu, L. Song, J. Zhu, Y. Xiong, Refining defect states in $\text{W}_{18}\text{O}_{49}$ by Mo doping:
27 A strategy for tuning N_2 activation towards solar-driven nitrogen fixation, *J. Am.
Chem. Soc.*, 140 (2018) 9434-9443.
- 29 [52] Z. Lou, P. Zhang, J. Li, X. Yang, B. Huang, B. Li, Plasmonic heterostructure TiO_2 -
30 MCs/ WO_{3-x} -NWs with continuous photoelectron injection boosting hot electron for
31 methane generation, *Adv. Funct. Mater.*, 29 (2019) 1808696.
- 32 [53] J. Zhou, X. An, Q. Tang, H. Lan, Q. Chen, H. Liu, J. Qu, Dual channel construction
33 of WO_3 photocatalysts by solution plasma for the persulfate-enhanced
34 photodegradation of bisphenol A, *Appl. Catal. B Environ.*, 277 (2020) 119221.

- 1 [54] J. Zhu, S. Pang, T. Dittrich, Y. Gao, W. Nie, J. Cui, R. Chen, H. An, F. Fan, C. Li,
2 Visualizing the nano cocatalyst aligned electric fields on single photocatalyst
3 particles, *Nano Lett.*, 17 (2017) 6735-6741.
- 4 [55] T. Wei, Y.-N. Zhu, Z. Gu, X. An, L.-m. Liu, Y. Wu, H. Liu, J. Tang, J. Qu, Multi-
5 electric field modulation for photocatalytic oxygen evolution: Enhanced charge
6 separation by coupling oxygen vacancies with faceted heterostructures, *Nano*
7 *Energy*, 51 (2018) 764-773.
- 8 [56] L.-W. Huang, T.-G. Vo, C.-Y. Chiang, Converting glycerol aqueous solution to
9 hydrogen energy and dihydroxyacetone by the BiVO₄ photoelectrochemical cell,
10 *Electrochim. Acta*, 322 (2019) 134725.
- 11 [57] P. Yang, J. Pan, Y. Liu, X. Zhang, J. Feng, S. Hong, D. Li, Insight into the role of
12 unsaturated coordination O_{2c}-Ti_{5c}-O_{2c} sites on selective glycerol oxidation over
13 AuPt/TiO₂ catalysts, *ACS Catal.*, 9 (2019) 188-199.
- 14 [58] Y. Zhou, Y. Shen, J. Xi, Seed-mediated synthesis of Pt_xAu_y@Ag electrocatalysts
15 for the selective oxidation of glycerol, *Appl. Catal. B Environ.*, 245 (2019) 604-
16 612.
- 17 [59] H. Tateno, S. Iguchi, Y. Miseki, K. Sayama, Photo-electrochemical C–H bond
18 activation of cyclohexane using a WO₃ photoanode and visible light, *Angew. Chem.*
19 *Int. Ed.*, 57 (2018) 11238-11241.
- 20 [60] D. Pan, S. Xiao, X. Chen, R. Li, Y. Cao, D. Zhang, S. Pu, Z. Li, G. Li, H. Li,
21 Efficient photocatalytic fuel cell via simultaneous visible-photoelectrocatalytic
22 degradation and electricity generation on a porous coral-like WO₃/W
23 photoelectrode, *Environ. Sci. Technol.*, 53 (2019) 3697-3706.